Enhanced Turbulence Associated with the Diurnal Jet in the Ocean Surface Boundary Layer

GRAIG SUTHERLAND,[a,b] LOUIS MARIÉ,[c] GILLES REVERDIN,[d] KAI H. CHRISTENSEN,[e] GÖRAN BROSTRÖM,[f] AND BRIAN WARD[b]

[a] *Department of Mathematics, University of Oslo, Oslo, Norway*
[b] *School of Physics, and the Ryan Institute, National University of Ireland, Galway, Ireland*
[c] *Laboratoire de Physique des Océans, CNRS/IFREMER/IRD/UBO, Plouzané, France*
[d] *LOCEAN Laboratory, Sorbonne Universités (UPMC, University of Paris 6)-CNRS-IRD-MNHN, Paris, France*
[e] *Norwegian Meteorological Institute, Oslo, Norway*
[f] *Department of Marine Sciences, University of Göteburg, Göteborg, Sweden*

ABSTRACT

Detailed observations of the diurnal jet, a surface intensification of the wind-driven current associated with the diurnal cycle of sea surface temperature (SST), were obtained during August and September 2012 in the subtropical Atlantic. A diurnal increase in SST of 0.2° to 0.5°C was observed, which corresponded to a diurnal jet of $0.15\,\mathrm{m\,s^{-1}}$. The increase in near-surface stratification limits the vertical diffusion of the wind stress, which in turn increases the near-surface shear. While the stratification decreased the turbulent dissipation rate ε below the depth of the diurnal jet, there was an observed increase in ε within the diurnal jet. The diurnal jet was observed to increase the near-surface shear by a factor of 5, which coincided with enhanced values of ε. The diurnal evolution of the Richardson number, which is an indicator of shear instability, is less than 1, suggesting that shear instability may contribute to near-surface turbulence. While the increased stratification due to the diurnal heating limits the depth of the momentum flux due to the wind, shear instability provides an additional source of turbulence that interacts with the enhanced shear of the diurnal jet to increase ε within this shallow layer.

1. Introduction

Many processes in the ocean surface boundary layer (OSBL) vary with the diurnal cycle of solar heating and nighttime cooling. The most frequently studied is that of sea surface temperature (SST), which is most pronounced under conditions of low winds and high solar insolation (e.g., Ward 2006). The diurnal variability of SST can be several degrees Celsius and has been shown to affect air–sea fluxes on climatological time scales in subtropical regions (Bernie et al. 2005; Kawai and Wada 2007; Clayson and Bogdanoff 2013). In addition to SST, diurnal variability has been observed in sea surface salinity (Drushka et al. 2014; Asher et al. 2014), momentum and shear (Weller and Plueddemann 1996; Plueddemann and Weller 1999; Cronin and Kessler 2009; Weller et al. 2014), and biogeochemical tracers such as dissolved oxygen and chlorophyll (Nicholson et al. 2015). In comparison, the diurnal variability of turbulence has received far less attention, although it is a key physical component the OSBL.

Diurnal restratification has been observed to reduce the dissipation rate of turbulent kinetic energy (ε; see section 3c for definition) below the restratification layer, leaving behind a remnant layer that is isolated from the surface wind stress (Brainerd and Gregg 1993; Caldwell et al. 1997; Callaghan et al. 2014). Restratification limits the vertical diffusion of the surface wind stress and thus causes the momentum flux to be focused to a shallower layer, causing it to slide with minimal friction (Kudryavtsev and Soloviev 1990). The magnitude of the diurnal jet is typically $O(10)\,\mathrm{cm\,s^{-1}}$ and extends to a depth of a few meters (Price et al. 1986; Woods and Strass 1986). Kelvin–Helmholtz (KH) instabilities have

Corresponding author address: Graig Sutherland, Department of Mathematics, University of Oslo, Postboks 1053 Blindern, 0316 Oslo, Norway.
E-mail: graigors@math.uio.no

been observed to form from the enhanced shear due to the diurnal jet and may be a source of active turbulence (Woods 1968; Soloviev and Lukas 2014).

While there exist many studies that have investigated the response of ε to a destabilizing buoyancy flux (Shay and Gregg 1986; Lombardo and Gregg 1989) and below the diurnal jet (Lombardo and Gregg 1989; Brainerd and Gregg 1993; Caldwell et al. 1997), there have been no studies that the authors are aware of that have investigated the variability of ε within the diurnal jet. If shear instabilities are common, as suggested by Woods (1968), this would provide a source of turbulent kinetic energy (TKE), which would enhance air–sea transfer of moderately soluble gases, such as CO_2 and O_2 (Lamont and Scott 1970; Jähne and Haußecker 1998; McGillis et al. 2004; Zappa et al. 2007), relative to wind-based parameterizations. Experiments by Khoo and Sonin (1992) demonstrated an appreciable increase in the mass transfer of CO_2 due to an increase in turbulence on the water side with zero interfacial shear or wave motion. As diurnal cycles of SST occur predominantly in low and midlatitudes, regions with a positive δpCO_2 (the partial pressure of the CO_2 in the air minus the partial pressure of CO_2 in the water) and hence a source of CO_2 to the atmosphere (Takahashi et al. 2009), enhanced turbulence associated with the diurnal jet would act to increase outgassing in these regions.

The diurnal jet in the ocean is analogous to that of the nocturnal jet in the atmosphere, also known as the low-level jet, as both consist of inertial rotations due to a diurnally varying buoyancy flux. However, there are a few key differences that could have large consequences for the dynamics. The nocturnal jet in the atmosphere is generated above the frictional stress layer during nocturnal cooling of the surface layer. This leads to an inertial oscillation generated due to frictional decoupling of the geostrophic forcing (Gill 1982). This mechanism suggests that the low-level jet only requires a nocturnal inversion to occur and will be independent of the wind and the nocturnal boundary layer depth. The diurnal jet in the ocean, on the other hand, is different in that it exists within the stress layer. Therefore, it is expected that the diurnal jet should exist as a wind-driven current that will rotate with the local inertial frequency (Price et al. 1986) and not as a free inertial oscillation (Gill 1982), although inertial oscillations could theoretically be generated from the diurnal variability in the OSBL thickness (D'Asaro 1985).

The motivation for this paper is to investigate the turbulent dynamics within the diurnal jet. What is the effect of the diurnal on the near-surface turbulence? Does the increase in shear due to the diurnal jet increase production of turbulent kinetic energy or does gravity limit

the vertical diffusion of the Reynolds stress? Is the diurnal jet susceptible to shear instability? This paper will attempt to address some of these questions with regards to the diurnal increase in stratification and the diurnal jet.

The outline for the paper is as follows: Section 2 provides an overview of the diurnal processes in the OSBL. Data and methods are presented in section 3. Section 4 shows the diurnal variability of temperature and velocity over the duration of the experiment. The diurnal structure of the observations was investigated using a composite day, which is calculated from phase averaging the forcing and ocean response as a function of the local time of day in section 5. An investigation of the relevant depth scale along with comparisons of previous results is shown in section 6. Section 7 presents statistics of the Richardson number, and section 8 investigates the large values of ε near the surface. A summary and discussion of the results are presented in section 9.

2. Overview of diurnal evolution of ε

The diurnal evolution of ε in the OSBL is primarily controlled by the varying surface buoyancy flux of solar heating during the day and surface cooling during the night (Price et al. 1986). The convective cycle during the night has been well described by similarity theory (Shay and Gregg 1986; Lombardo and Gregg 1989), while the details of the stable daytime stratification regime are still relatively unknown due to the lack of observations in these shallow stable layers (Soloviev and Lukas 2014). Presented in this section is a short summary of the diurnal cycle outlining some of the larger gaps in current understanding.

The OSBL is highly turbulent with the energetics being quantified by the time evolution of TKE. Assuming the flow is horizontally homogeneous, the vertical structure of TKE in the OSBL can be written as (Belcher et al. 2012)

$$\frac{dq}{dt} = \underbrace{u_*^2\frac{\partial U}{\partial z}}_{(a)} + \underbrace{u_*^2\frac{\partial U_s}{\partial z}}_{(b)} + \underbrace{\overline{w'b'}}_{(c)}$$
$$+ \underbrace{\frac{\partial}{\partial z}\left(\overline{w'u_i'u_i'} + \frac{1}{\rho_0}\overline{w'p'}\right)}_{(d)} + \underbrace{\varepsilon}_{(e)}, \quad (1)$$

where q is the TKE, u_* is the friction velocity in water, U is the mean horizontal current, U_s is the Stokes drift, ρ_0 is the density of seawater, and b', p', and u_i' are turbulent fluctuations in buoyancy, pressure, and velocity, respectively, where $w' = u_3'$ is the vertical turbulent velocity. The buoyancy fluctuation is defined as $b' = g\rho'/\rho_0$.
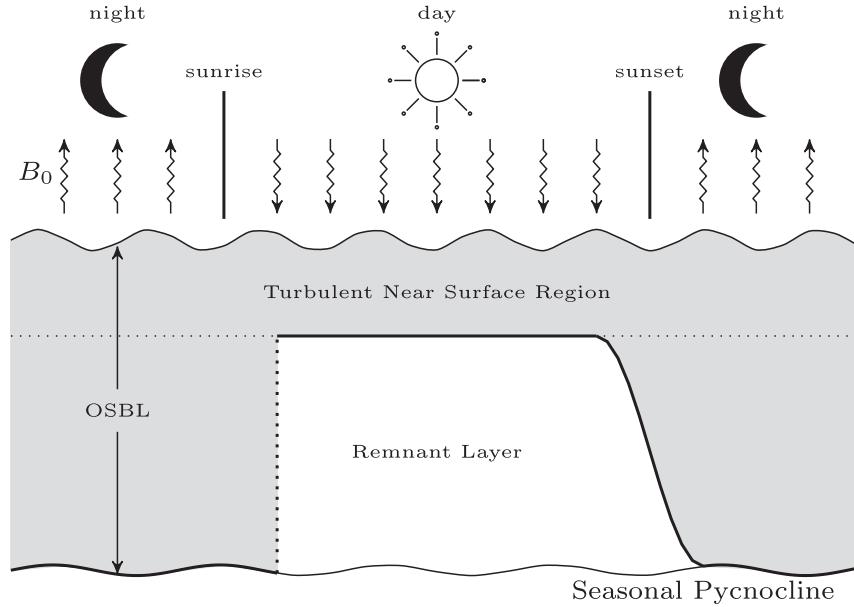
FIG. 1. Schematic of the diurnal cycle of turbulence. The shaded region represents the OSBL. The turbulent near-surface region is the depth at which turbulent production is greater than the buoyancy flux.

The time evolution of TKE that can be seen in (1) is the sum of the (a) = mean shear production, (b) = production from the Stokes shear, (c) = buoyancy flux, (d) = transport of TKE and (e) = the dissipation rate of TKE due to viscosity. In (1), terms (a) and (b) are sources of TKE, (c) can be a source or sink depending on the surface buoyancy flux and the amount of mixing, (d) redistributes TKE and is neither a source or a sink, and (e) is a sink for TKE. In the constant stress layer near the ocean surface, $u_* = \sqrt{\tau/\rho_0}$, where τ is the surface wind stress, and $\overline{w'b'} \approx B_0$, where B_0 is the surface buoyancy flux.

In the OSBL, TKE is generally considered to be in a quasi-steady state (Osborn 1980) with ε being balanced by the sum of shear production and buoyancy fluxes. The length scale at which shear production, assuming a logarithmic velocity profile, and buoyancy are balanced is known as the Monin–Obukhov length (Gill 1982), defined as

$$L_{\mathrm{MO}} = -\frac{u_*^3}{\kappa B(z)}, \tag{2}$$

where $\kappa = 0.4$ is the von Kármán constant, and $B(z)$ is the depth-dependent buoyancy flux to an OSBL thickness of z and is defined as

$$B(z) = B_t + [B_R(0) - B_R(z)], \tag{3}$$

where $B_R(z)$ is the depth-dependent shortwave component of the buoyancy flux, and B_t is the turbulent

component that includes latent and sensible heat and infrared radiation, as this does not penetrate greater than 1 cm in the ocean (Soloviev and Lukas 2014).

A schematic of the diurnal cycle is depicted in Fig. 1. For depths less than L_{MO}, shear turbulence dominates buoyancy forces, and this region is denoted by the turbulent near-surface region in Fig. 1. Cooling at night causes the surface layer to be gravitationally unstable, generating convection cells that extend to the seasonal pycnocline, creating a well-mixed OSBL (Shay and Gregg 1986). Ocean convection has been well studied, and it has been shown that $\varepsilon \propto B_0$ below the near-surface turbulent region (Shay and Gregg 1986).

In the morning, the rising sun provides a stabilizing buoyancy flux into the OSBL. This buoyancy flux varies with depth (Paulson and Simpson 1977) and, under favorable wind conditions, the near surface of the ocean will begin to restratify. The depth to which significant heating occurs is expected to be related to L_{MO} (Kudryavtsev and Soloviev 1990; Large et al. 1994). Below this restratification depth, a remnant layer exists that is isolated from surface wind forcing (Brainerd and Gregg 1993). A decrease in ε is observed in this remnant layer with an exponential decay in time (Brainerd and Gregg 1993; Caldwell et al. 1997; Callaghan et al. 2014).

Within the OSBL, ε can be modeled as a function of the friction velocity u_* and surface buoyancy flux B_0 (Lombardo and Gregg 1989), which we will denote ε_0, where

$$\varepsilon_0 = a\frac{u_*^3}{\kappa|z|} + b\frac{B_0 + |B_0|}{2}, \qquad (4)$$

and a and b are constants. Typical ranges for the constants a and b are $0.5 < a < 2$ and $0.3 < b < 2$ (Shay and Gregg 1986; Lombardo and Gregg 1989; Brainerd and Gregg 1993; Caldwell et al. 1997; Callaghan et al. 2014). Equation (4) states that ε_0 will be greater by an offset proportional to B_0 relative to shear production during convection and that ε will not be affected by the buoyancy flux during restratification. Equation (4) only applies to the constant stress layer, which can be very shallow during restratification, and may not apply to the remnant layer (Callaghan et al. 2014). Measuring the depth dependence of the Reynolds stress in the OSBL is difficult due to the spectral overlap of turbulent motions and surface wave orbital motion (D'Asaro 2014). In general, the constant stress layer depth is assumed to be the same as the mixed layer depth, but there is little evidence for this, especially for variability on short time scales (Sutherland et al. 2014b). There have been some efforts to define the OSBL using ε, rather than based on density homogeneity, as this should scale more closely with u_*, with some promising results for high-resolution studies (Brainerd and Gregg 1995; Sutherland et al. 2014a,b).

Equation (4) only accounts for surface forcing due to the wind stress and surface buoyancy flux and does not account for other processes that could affect ε such as breaking waves (Craig and Banner 1994), Langmuir circulations (McWilliams et al. 1997; Belcher et al. 2012), shear instabilities (Woods 1968), horizontal processes associated with ocean fronts (D'Asaro et al. 2011), or breaking internal waves (Wain et al. 2015), to name a few. These processes all generate TKE, which would lead to an underestimation of ε relative to (4).

3. Data and methods

Observations of the OSBL were obtained during the Subtropical Atlantic Surface Salinity Experiment (STRASSE) aboard the *Navire Océanographique* (N/O) *Thalassa* (Reverdin et al. 2015). This experiment took place during August and September 2012 as part of the larger Salinity Processes in the Upper Ocean Regional Study (SPURS) project. The location of the experiment is shown in Fig. 2. The latitude of the experiment site was about 25.6°N, corresponding to an inertial period of 27.7 h.

a. Meteorological observations

Radiative fluxes and wind speed measurements were recorded aboard the N/O *Thalassa*. The wind stress and buoyancy flux were calculated using the TOGA COARE
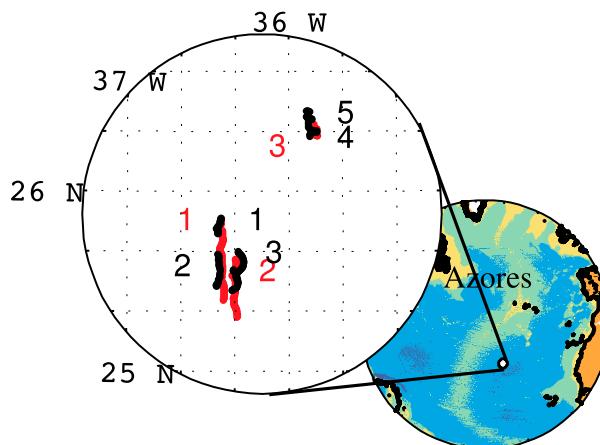
FIG. 2. Location for the five ASIP deployments (shown in black) and three Trèfle deployments (shown in red) during late August–early September 2012.

3.0 algorithm (Fairall et al. 2003). Figure 3a shows the 10-m wind speed U_{10}, direction U_{DIR}, and B_0. The wind speed varied between 2 and $10\,\mathrm{m\,s^{-1}}$ with directions ranging between predominantly from the north to easterly. The surface buoyancy flux followed a typical pattern of surface cooling at night and heating during the day.

b. Wave and current observations

Observations of surface gravity waves and velocity profiles were made with a cloverleaf buoy, the Trèfle, equipped with a downward-facing Teledyne RD Instruments 300-kHz acoustic Doppler current profiler (ADCP), an MTi-G global positioning system (GPS)–motion sensor package manufactured by Xsens, and a Nortek Vector velocimeter mounted at 0.5-m depth to obtain the near-surface velocity. The buoy was tethered to a surface velocity program (SVP) drifter with a 50-m drogue in order to reduce its windage-induced drift. A custom datalogger performed collection and consistent time stamping of the three data streams. The ADCP profiled from 3.5 to 78.5 m with a 1-m depth resolution and an effective range of roughly 75 m.

Wave motions were quantified using the xSens MTI-G GPS motion sensor package, which consists of a GPS and a 6 degrees of freedom inertial motion unit (IMU) sampled at 10 Hz. The GPS and IMU compose an attitude heading reference system (AHRS) that utilizes a Kalman filter to combine the inertial motions and GPS position. The vertical motion was subsequently bandpass filtered using a fourth-order Chebyshev type-II filter with a 40-dB stop band ripple and cutoff frequencies 0.025 and 3 Hz, applied forwards and then backward to eliminate phase delay, resulting in an eighth-order, 80-dB ripple filter. One-dimensional
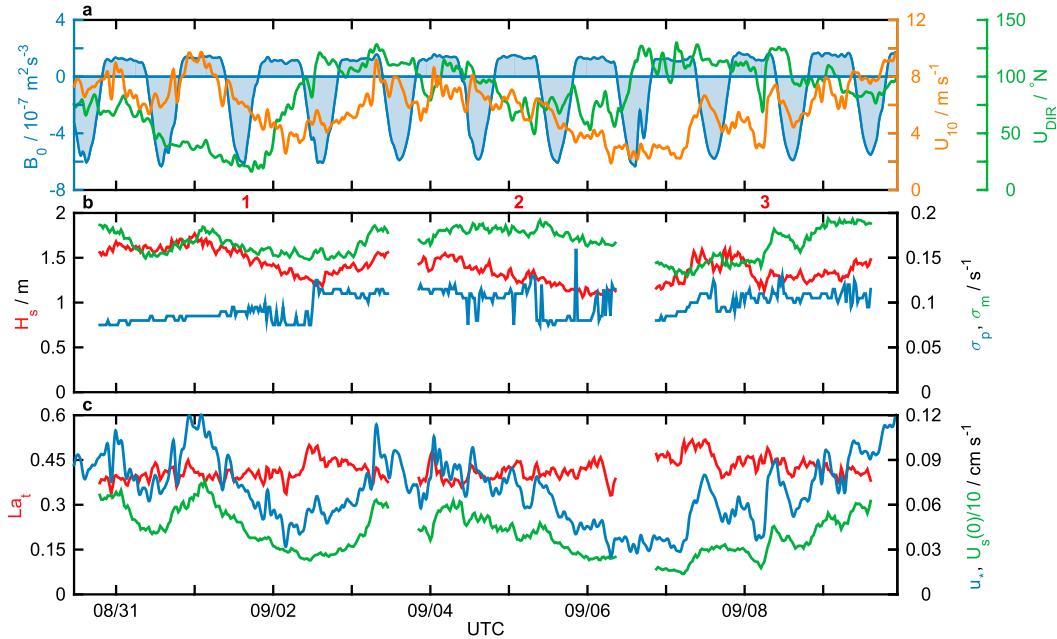
FIG. 3. Time series of observations for (a) surface buoyancy flux B_0 (blue), wind speed U_{10} (orange), and direction U_{DIR} (green); (b) significant wave height H_s (red), peak frequency σ_p (blue), and mean frequency σ_m (green); and (c) the turbulent Langmuir number La (red), the friction velocity u_* (blue), and the surface Stokes drift divided by 10 [$U_s(0)/10$; green]. The Trèfle deployment numbers corresponding with the wave observations are shown in red above (b).

wave spectra were calculated every 30 min from the AHRS heave. The calculated significant wave height H_s, peak frequency σ_p, and mean frequency σ_m are shown in Fig. 3b.

The Stokes drift as a function of depth can be calculated from the 1D wave spectrum (Kenyon 1969) as

$$U_s(z) = \frac{16\pi^3}{g} \int_{\sigma_{min}}^{\sigma_{max}} \sigma^3 S(\sigma) e^{(4\pi^2\sigma^2/g)z} \, d\sigma, \quad (5)$$

where σ is the frequency, $S(\sigma)$ is the 1D wave spectrum, and σ_{min} and σ_{max} are the cutoff frequencies chosen as 0.05 and 0.50 Hz, respectively. There are two opposing uncertainties with calculating the Stokes velocity from a 1D wave spectrum using a finite frequency range: the lack of a measured high-frequency spectral tail and the lack of the directional spreading of the wave energy. The former will lead to a systematic underestimate of $U_s(0)$ up to 30% (Rascle et al. 2006), with the exact amount dependent on the slope of the spectral tail, while the latter leads to a systematic overestimate of $U_s(0)$ up to 30% (Webb and Fox-Kemper 2011), dependent on the directional spread of wave energy. Lacking measurements of both the high-frequency component of the wave spectrum and directional information, we assume that the effects on the Stokes drift should approximately cancel each other. This assumption has been used in

previous studies (Gargett and Grosch 2014; Sutherland et al. 2014a) and has the advantage of estimating $U_s(0)$ only from observations and not artificially adding a high-frequency component to the wave spectrum.

The surface Stokes velocity was used in conjunction with u_* to calculate the turbulent Langmuir number $La_t = \sqrt{u_*/U_s(0)}$, which is used as a proxy for turbulence associated with Langmuir circulations (McWilliams et al. 1997). Figure 3c shows the time series for $U_s(0)$, u_*, and La_t. Langmuir turbulence is expected to occur when $La_t < 0.3$ (McWilliams et al. 1997), which is not fulfilled during our observations. We therefore neglect Langmuir circulations as a dominant mechanism for turbulence in our observations.

Velocities in the OSBL are presented relative to a reference depth of $z_0 = 40$ m located just below the seasonal mixed layer, that is,

$$u(z,t) = U(z,t) - U_0(t), \quad (6)$$
$$v(z,t) = V(z,t) - V_0(t), \quad (7)$$

where the 0 subscript denotes the velocity at the reference depth. Figure 4 shows the mean currents at 40 m along with the velocity anomalies relative to this current. The orthogonal velocity components are arranged in an along-wind U and across-wind V component, where the V axis is 90° clockwise to U.
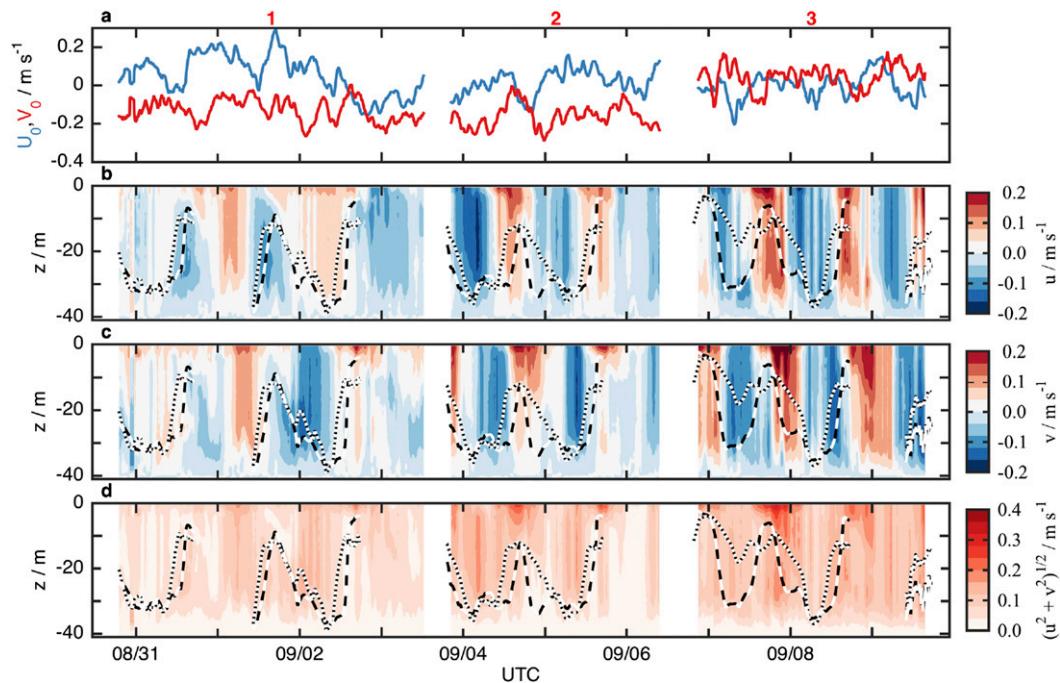
FIG. 4. Observations of near-surface currents from each of the three Trèfle deployments. (a) The mean velocity at 40 m, (b) the along-wind, (c) crosswind velocities relative to 40 m, and (d) the velocity magnitude relative to 40 m. The MLD and XLD are shown by the black–white dashed and dotted lines, respectively. The Trèfle deployment numbers corresponding with the wave observations are shown in red along the top. The magnitude changes little with the exception of the near-surface currents during the day.

Enhanced near-surface shear is observed every day, consistent with the diurnal jet phenomenon described by Price et al. (1986).

c. Microstructure measurements

Measurements of the turbulent dissipation rate, temperature, and salinity were obtained with the Air–Sea Interaction Profiler (ASIP; Ward et al. 2014). ASIP is an autonomous, upwardly rising microstructure profiler designed to sample the OSBL. A total of 347 profiles from 40-m depth to the surface were obtained over five ASIP deployments. Each deployment ranged from 24 to 48 h in duration with the exception of the fifth deployment, which was only 10 h. The average time between successive profiles during each deployment was about 20 min.

The time–depth evolution of temperature T and buoyancy frequency N^2 are shown in Fig. 5. The density ratio in the OSBL, defined by $R_\rho = (\alpha \partial T/\partial z)/(\beta \partial S/\partial z)$, where α and β are the thermal expansion coefficient and the saline contraction coefficient, respectively, and $\partial T/\partial z$ and $\partial S/\partial z$ are the vertical gradients of temperature and salinity, respectively, was typically greater than 2, indicative of temperature controlled stratification. In addition, the conductivity signal, from which salinity is calculated, in the upper 10 m was sometimes contaminated from the impact of near-surface detritus striking the conductivity probe, which acted to increase the noise in the measured salinity. Therefore, only the contribution from $\partial T/\partial z$ was used to calculate N^2 in the OSBL. Each profile of T was sorted to calculate the stable stratification and ensure $N^2 > 0$.

Dissipation rates of ε were measured using two airfoil shear probes mounted on the front of ASIP (Sutherland et al. 2013). Assuming isotropic turbulence, ε can be calculated from profiles of the microstructure shear (Osborn 1974). The microstructure shear was sampled at 1000 Hz, and vertical profiles were divided into 1-s segments where the power spectral density was calculated using Welch's method. The mean rise velocity of ASIP was $0.5\,\mathrm{m\,s}^{-1}$, thus giving a vertical resolution for ε of 0.5 m. Details of the processing algorithm for ε can be found in Ward et al. (2014). Figure 5e shows the measured turbulent dissipation rate for the five deployments. In addition, Fig. 5f shows ε normalized by ε_0, calculated by (4), which takes into account turbulence generated from the mean shear and convective buoyancy forcing. The constants a and b in (4) are found to $a = 0.5$ and $b = 0.3$, which is consistent with previous results (Shay and Gregg 1986; Lombardo and Gregg 1989; Brainerd and Gregg 1993; Caldwell et al. 1997; Callaghan et al. 2014).
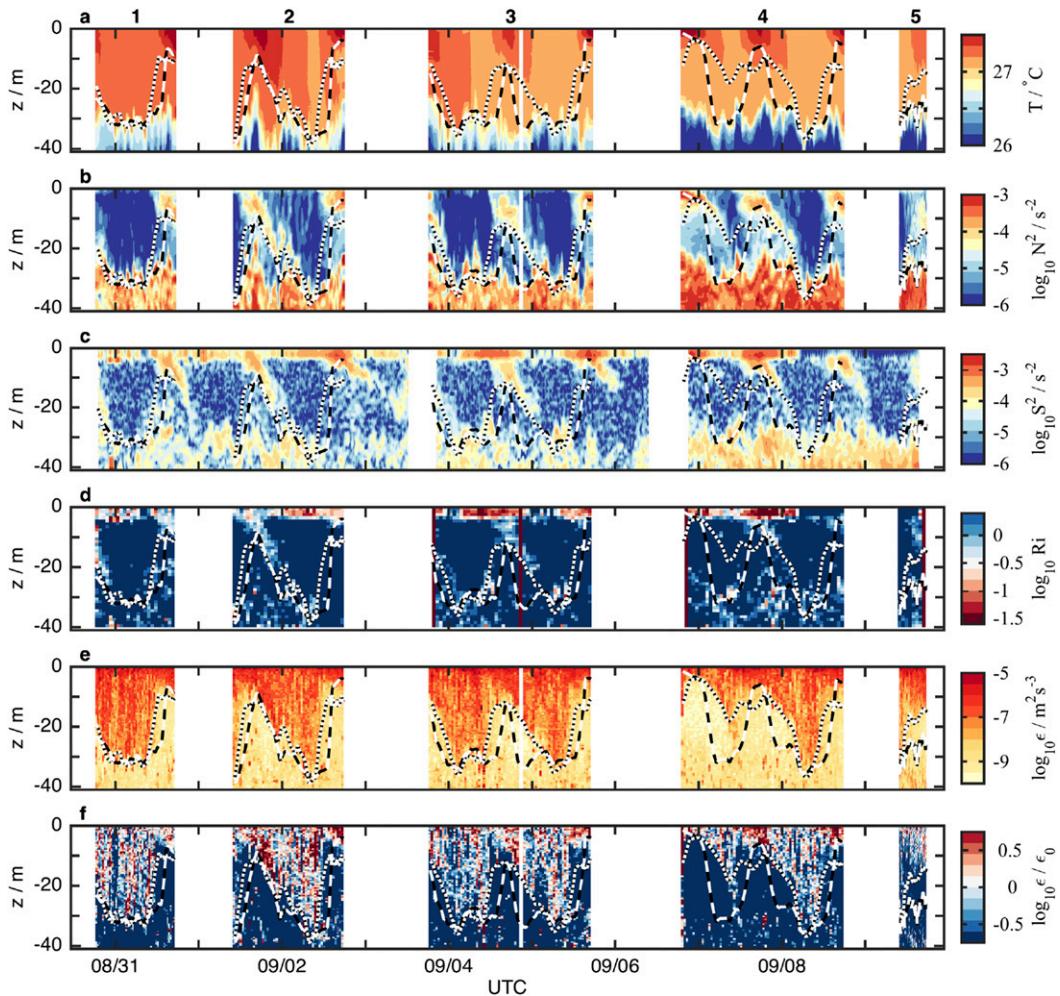
FIG. 5. Observations over the five ASIP deployments (numbered 1 to 5 along the top) of (a) temperature T and the $\log_{10}$ of the (b) Brunt–Väisälä frequency squared N^2, (c) shear squared S^2, (d) gradient Richardson number $\text{Ri} = N^2/S^2$, (e) turbulent dissipation rate ε, and (f) normalized turbulent dissipation rate $\varepsilon/\varepsilon_0$. The MLD and XLD are shown by the black–white dashed and dotted lines, respectively.

The mixed layer depth (MLD) was calculated using the temperature threshold of 0.2°C relative to the temperature at $z = -0.5\,\text{m}$ (Kara et al. 2000; de Boyer Montégut et al. 2004). The MLD over the five ASIP deployments is shown by the black–white dashed line in Fig. 5. The active mixing layer depth (XLD) is defined as the depth where ε decreases to an assumed background level and is no longer being influenced by surface forcing (Sutherland et al. 2014a). The XLD is calculated assuming a background dissipation of $10^{-9}\,\text{m}^{-2}\,\text{s}^{-3}$ (Sutherland et al. 2014b). Differences between the MLD and XLD have been shown to be important in scaling observations of ε with surface forcing (Brainerd and Gregg 1995; Stevens et al. 2011; Sutherland et al. 2014a). The XLD is indicated by the black–white dotted line in Fig. 5.

Mean values for the day and night profiles of temperature, current speed, ε, $\varepsilon/\varepsilon_0$, and $\text{Ri} = N^2/S^2$ are shown in Fig. 6. The geometric mean is used for ε, N^2, and S^2. The mean daytime profile was averaged over 1400–1600 local mean time (LMT), calculated such that noon coincides with the peak solar altitude and the nighttime profile was averaged over 0200–0400 LMT. During the day there is an increase in the near-surface temperature coinciding with an increase in the near-surface velocity to a depth of approximately 8 m. There is an associated enhanced ε in this depth range, while ε decreases by nearly two orders of magnitudes below the shallow restratification depth.

The day and night probability density function (PDF) and cumulative distribution function (CDF) of ε and ε_0 are shown in Fig. 7 for three different depth intervals
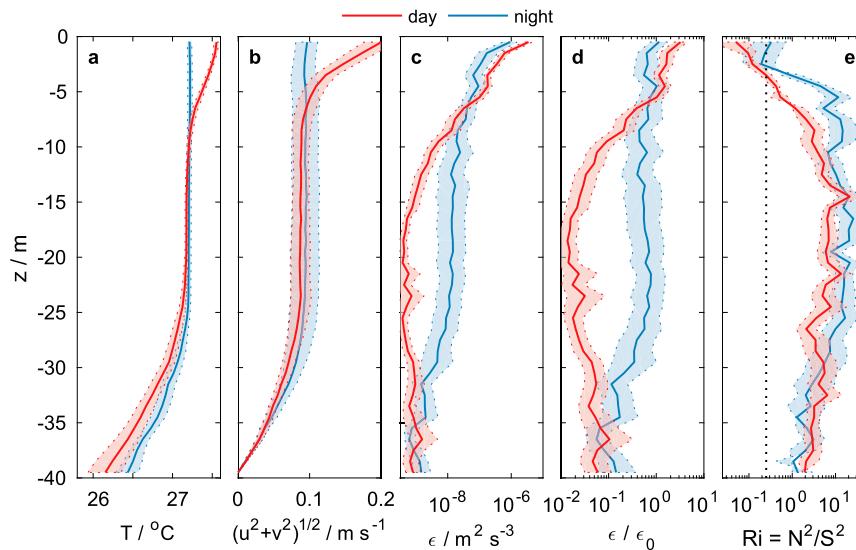
FIG. 6. Mean day (red) and night (blue) profiles of (a) temperature, (b) velocity magnitude, (c) ε, (d) $\varepsilon/\varepsilon_0$, and Ri $= N^2/S^2$. Night is defined between 0100 and 0400 LMT and day is 1300 to 1600 LMT. Shaded regions enclosed by the dotted lines represent 95% confidence intervals as calculated with a bootstrap method. Current and temperature vary between day and night in the upper 10 m, while ε is affected down to the seasonal pycnocline at approximately $z = -30$ m.

from the surface to -12 m. For depths from -4 m to the surface (Fig. 7a), ε is greater during the day than during the night with a median value that is 3 times greater. For the next depth interval (Fig. 7), the day and night distributions are very similar, with the night having a slightly larger peak and the day having a greater likelihood for values greater than the median. Below -8 m (Fig. 7), ε is most likely to be less during the day than in

the night. The PDF and CDF are also shown for ε_0 (Figs. 7d–f), demonstrating that there is no day–night bias in the upper part of the ocean.

4. Diurnal variability of temperature and velocity

We define the diurnal variability of temperature and velocity in the same manner as Price et al. (1986), that is,
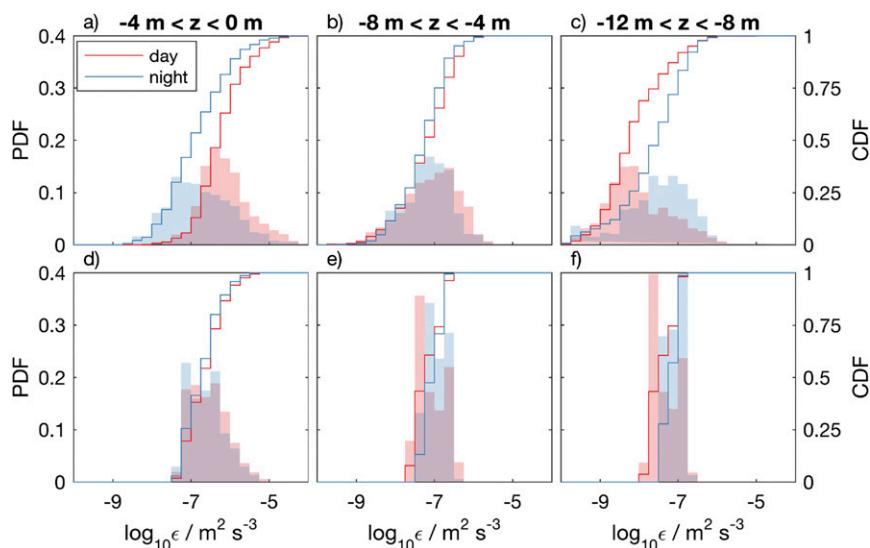
FIG. 7. PDF of (a),(b),(c) ε and (d),(e),(f) ε_0 for the day (red) and night (blue) times of Fig. 6 for (left) -4 m $< z < 0$ m, (middle) -8 m $< z < -4$ m, and (right) -12 m $< z < -8$ m The lines show the CDF with the corresponding scale on the right side of the figure.
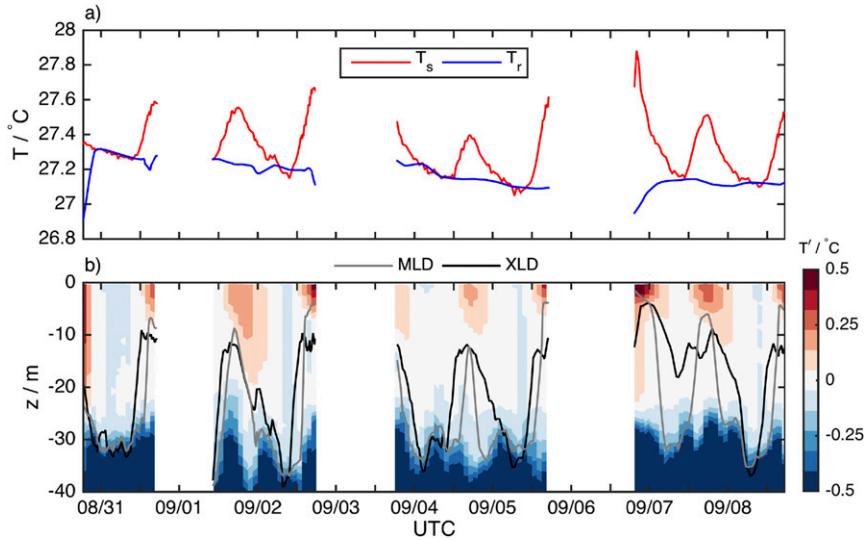
FIG. 8. (a) Temperature at $z_s = -0.5$ m (T_s, red) and $z_r = -25$ m (T_r, blue) and (b) $T' = T - T_r$ observed over the ASIP deployments. The black and gray lines in (b) are the XLD and the MLD, respectively. The diurnal variability in T_s was observed to be 0.2°–0.3°C and T' began descending in the early afternoon, approximately 1500 LMT, before the surface buoyancy flux changed sign.

$$T'(z,t) = T(z,t) - T_r(t), \qquad (8)$$

$$u'(z,t) = U(z,t) - U_r(t), \qquad (9)$$

$$v'(z,t) = V(z,t) - V_r(t), \qquad (10)$$

where the r subscript denotes a reference depth, which is chosen to be deep enough to avoid the diurnal signal and shallow enough to not include the seasonal pycnocline. From visual inspection of Fig. 5, a reference depth of $z_r = -25$ m is chosen. A median point filter with a sliding window of 2 h was applied to remove any spikes associated with the seasonal pycnocline contaminating the reference temperature.

Figure 8 shows the evolution of T_s, T_r, and T', where T_s is the surface temperature at a depth $z_s = -0.5$ m. The diurnal cycling of upper-ocean temperature is observed to increase in the near-surface temperature by 0.2°–0.5°C during the day. Figure 8a also shows the difficulty in determining a single reference depth as the seasonal pycnocline appears to contaminate $T_r(t)$ on 08/31 and 09/07. The diurnal cycle of T' is fairly typical over the ASIP deployments with shallow anomalies extending to deeper depths during the day until they are suddenly exterminated by the change to a destabilizing surface buoyancy flux.

Figure 9 shows the diurnal velocity variability over the three Trèfle deployments. The velocity anomalies begin in the along-wind direction in the morning and turn with the local inertial frequency during the day. The velocity anomaly has a similar pattern as the temperature anomaly in Fig. 8 where the anomaly begins in a shallow layer during the morning, descending in the afternoon, and is erased when the surface buoyancy flux becomes destabilizing.

The diurnal velocity response is more clearly seen in the surface velocity, which is averaged over the upper 5 m, as seen in Fig. 10. The magnitude of the diurnal jet is consistently observed to be approximately $0.15 \, \text{m s}^{-1}$. This near-uniform diurnal jet magnitude is consistent with the observations of Price et al. (1986), who found that the magnitude should only be dependent on the shortwave radiation and independent of the wind stress. However, there is day to day variability with regards to the timing of the peak of the diurnal jet in addition to the evolution of the along- and crosswind components (Fig. 10).

5. Composite day

Wind variability predominantly occurred over time scales greater than the diurnal period (Fig. 3), allowing for the creation of a single composite day by phase averaging the forcing and response components as functions of the local time of day. The composite day allows for a detailed analysis of the mean diurnal response of the ocean while filtering out processes that were not phase coherent within the diurnal cycle. This method has proven useful in interpreting the mean diurnal response in regions with strong buoyancy forcing (Caldwell et al. 1997; Smyth et al. 2013; Drushka et al. 2014; Sutherland et al. 2014b).
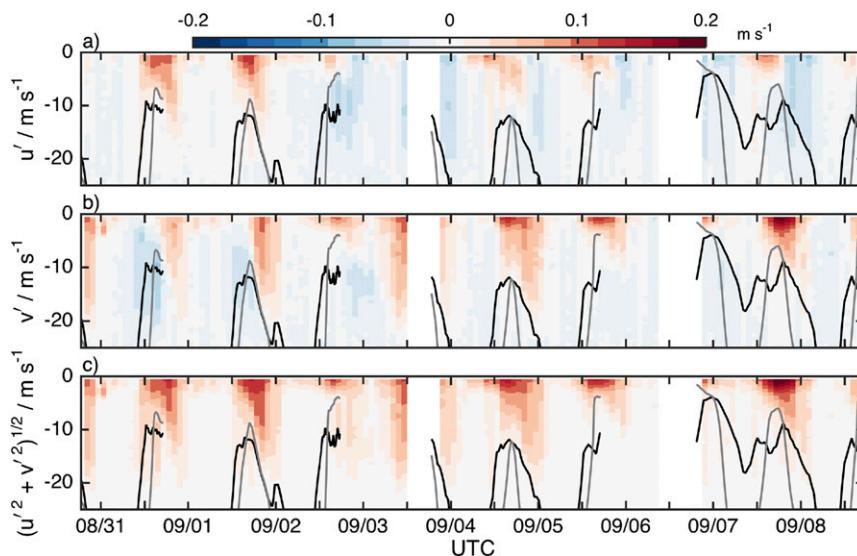
FIG. 9. Diurnal velocity anomalies relative to $z_r = -25$ m, identical to the calculation of T', for the (a) along-wind component u', (b) crosswind component v', and (c) the magnitude of the velocity vector $(u'^2 + v'^2)^{1/2}$. The gray lines show the MLD and the black lines show the XLD. The time–depth variability of $(u'^2 + v'^2)^{1/2}$ is similar to T' (Fig. 8), which is consistent with having similar diffusivities for temperature and momentum.

Figure 11 shows the composite day for the surface forcing and ocean response. The phase averaging was performed with a temporal resolution of 1 h and a depth resolution of 1 m. The phase-averaged surface buoyancy flux B_0 and wind stress τ are shown in Fig. 11a. The

surface buoyancy flux had a clear diurnal structure with little observed variation. Although the wind speed varied from 2 to 10 m s^{-1} over all the deployments (Fig. 3a), there was no clear diurnal structure in τ around the mean value of 0.06 N m^{-1} (Fig. 11a).
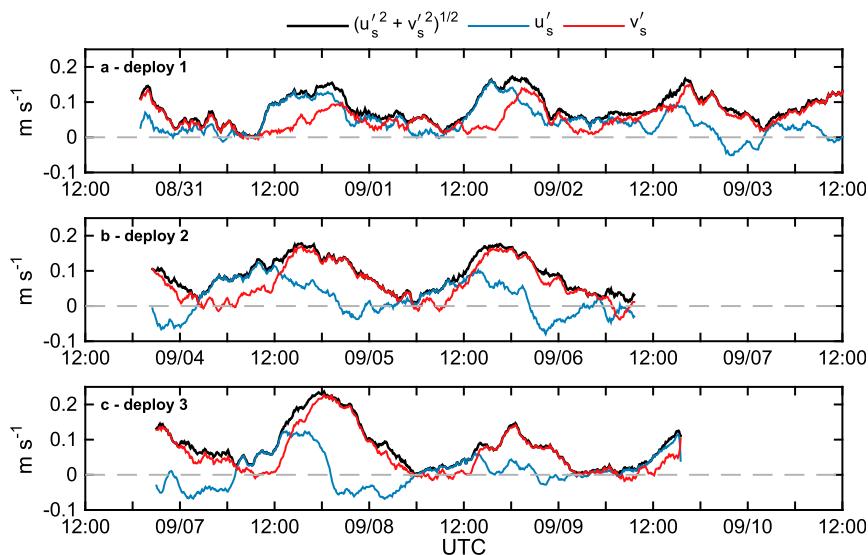
FIG. 10. Diurnal jet calculated from the observed velocity (black) averaged over the upper 5 m relative to the velocity at 25 m, where u'_s (blue) and v'_s (red) are the along-wind and crosswind anomalies of the surface velocity, respectively: (top to bottom) deployments 1, 2, and 3. The x axis has both month/day and time (UTC). The diurnal jet rotated clockwise with a maximum magnitude consistently around 0.15 m s^{-1}, while the relative magnitudes of the along-wind and crosswind components varied between each day.
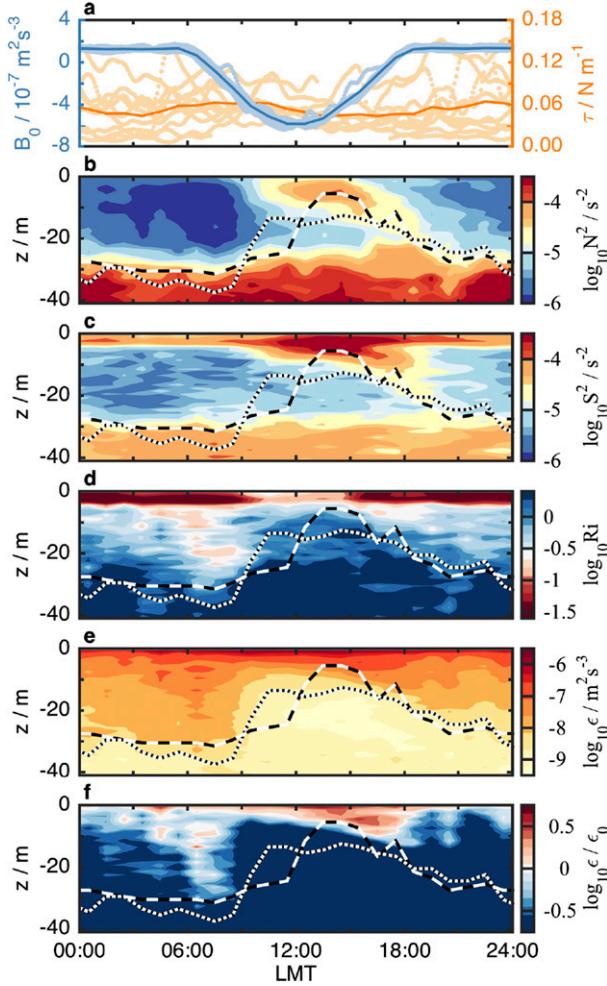
FIG. 11. Composite day for (a) B_0 (blue) and τ (orange) and the $\log_{10}$ of (b) N^2, (c) S^2, (d) Ri, (e) ε, and (f) $\varepsilon/\varepsilon_0$ vs LMT. The MLD (black–white dashed) and XLD (black–white dotted) are calculated from the composite values of T and ε.

The near-surface stratification N^2 (Fig. 11b) and shear squared S^2 (Fig. 11c) were both observed to increase after B_0 became stabilizing, with N^2 lagging S^2 by a few hours. Both N^2 and S^2 reached near-surface maxima at close to 1400 LMT after which these maxima descended to greater depths. In the afternoon as the depth of the OSBL increased, the magnitude of N^2 and S^2 both decreased.

As an indicator for shear stability, the gradient Richardson number was calculated:

$$\text{Ri} = \frac{N^2}{S^2}, \tag{11}$$

where N^2 and S^2 are composite day values, similar to the composite Ri presented by Smyth et al. (2013). When Ri falls below a critical value of 0.25, the flow may become

unstable (Miles 1961). Figure 11d shows the logarithm of Ri centered on $\log_{10} 0.25 = -0.60$, such that the red values correspond to where shear instability was likely to occur.

6. Restratification length scale

Price et al. (1986) introduced two diagnostic depth scales associated with restratification, which they called the trapping depth D_T and penetration depth D_P. The trapping depth is defined as the mean depth of the temperature anomaly in the OSBL, where the temperature anomaly is defined in (8).

The trapping depth is calculated from the vertical integral of (8), that is,

$$D_T = \frac{1}{T_s'} \int_{z_r}^{z_s} T' \, dz, \tag{12}$$

where z_s is the surface depth, which we take to be $z_s = -0.25$ m, and $T_s' = T'(z_s, t)$. Equation (12) incorporates the diurnal heat anomaly normalized by the surface temperature.

The penetration depth, on the other hand, is the depth scale in the one-dimensional heat equation, that is,

$$\frac{\partial T}{\partial t} = -\frac{1}{\rho_0 c_p} \frac{\partial Q_0}{\partial z}, \tag{13}$$

where c_p is the specific heat of seawater, and Q_0 is the surface heat flux, which can be related to the surface buoyancy flux $B_0 = g\alpha Q/(\rho_0 c_p)$, and c_p is the specific heat of seawater. Price et al. (1986) calculated the penetration depth to be

$$D_P = \frac{Q_0}{\rho_0 c} \left(\frac{\partial T_s'}{\partial t} \right)^{-1}. \tag{14}$$

The penetration depth can be interpreted as the depth to which mixing from surface forcing is present, assumed by Price et al. (1986) to be entirely derived from the wind.

The trapping and penetration depths were also calculated from the composite day values of T and Q, as shown in Fig. 12. Before 1200 LMT, the minimum D_P was very similar to the minimum D_T, suggesting that heat and momentum are mixed in the same manner, consistent with Price et al. (1986). At 1200 LMT, $D_T = D_P = 10$ m, which is larger than L_{MO} but similar in magnitude to the minimum MLD and XLD (Fig. 12).

Another depth scale associated with restratification is the prognostic depth scale of Price et al. (1986):
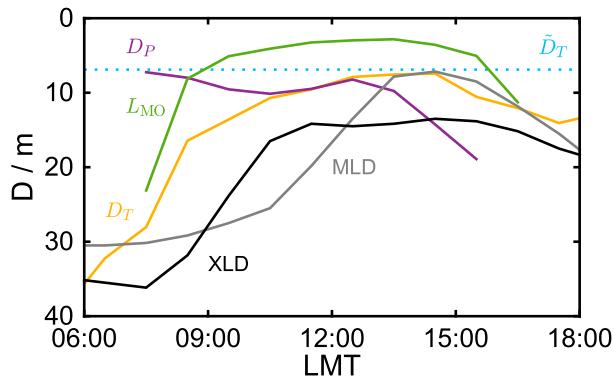
FIG. 12. Depth scales associated with restratification calculated from the composite day. Depths include the Monin–Obukhov length L_{MO} (green), penetration depth D_P (purple), trapping depth D_T (yellow), the MLD (gray), XLD (black), as well as $\tilde{D}_T$ (light blue dotted).

$$\tilde{D}_T = 0.45 \frac{\tau}{\rho_0 B_0^{1/2}} \frac{P_\tau}{P_Q^{1/2}} J^{-3/2}, \qquad (15)$$

where P_Q is the time scale associated with the buoyancy flux, taken to be half the length of the duration of stabilizing buoyancy flux; $P_\tau = f^{-1}[2 - 2\cos(fP_Q)]^{1/2}$ is the acceleration time scale that accounts for rotation; and J is associated with the depth penetration of shortwave radiation. For the composite day there is good agreement between $\tilde{D}_T$ and the minimum values of D_T, D_P, and MLD (Fig. 12). The minimum XLD thickness is greater than $\tilde{D}_T$ by a factor of 2, which will ultimately be associated with how the XLD is defined. Better agreement between $\tilde{D}_T$ and the XLD is obtained if the background threshold is increased by a factor of 5 (not shown), but this threshold greatly underpredicts the boundary thickness during the night.

For mid to low latitudes where diurnal cycling is prominent, $P_Q \approx P_\tau$ and $\tilde{D}_T$ can be written in terms of L_{MO}, that is,

$$\tilde{D}_T \propto (L_{MO})^{1/2}(u_* P_Q)^{1/2}. \qquad (16)$$

Assuming that an external time scale is not necessary to determine $\tilde{D}_T$ allows for P_Q to be replaced by L_{MO}/u_* in (16), leading to the Monin–Obukhov scaling of $\tilde{D}_T \propto L_{MO}$. It is clear from Fig. 12 that $\tilde{D}_T > L_{MO}$ and that the time scale associated with solar heating should be taken into account.

Figure 12 shows that L_{MO} not only underestimates the depth of the boundary layer, but it does not demonstrate any of the temporal variability as shown by the MLD and XLD. It appears that mean values of u_* and B_0 alone are insufficient to calculate the scale of the
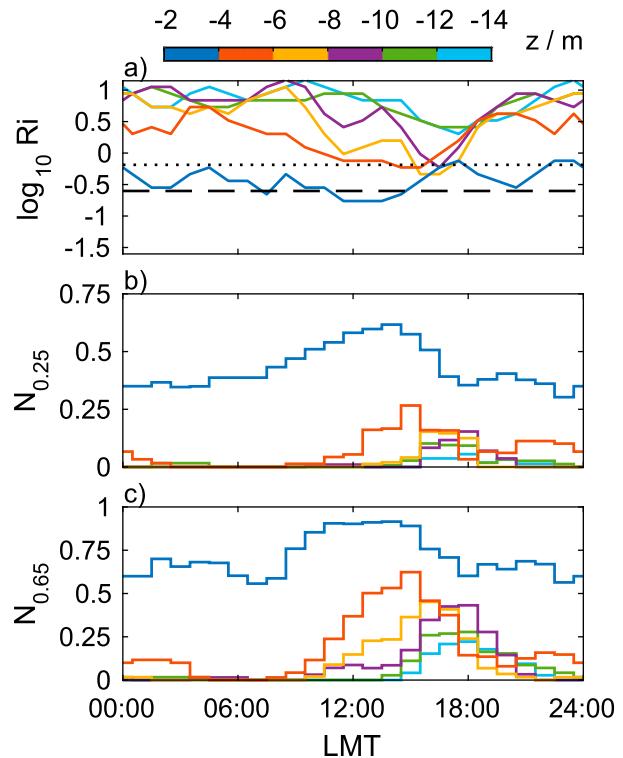
FIG. 13. Diurnal evolution of (a) the $\log_{10}$ of the peak Richardson number associated with the PDF calculated for each hour of the composite day, (b) the fraction of observed values of Ri < 0.25, and (c) the fraction of observed values of Ri < 0.65. The colors denote the different depth intervals as shown by the legend at the top. The dashed and dotted lines in (a) show Ri = 0.25 and 0.65, respectively. The local minima in the mode during the day correspond with a greater occurrence of low Richardson numbers.

boundary layer depth, and a relevant time scale, such as proposed by Price et al. (1986), is necessary to obtain the correct magnitude.

7. Richardson number statistics

The gradient Richardson number, where Ri is defined by (11), is calculated for each profile and the statistical distribution as a function of local time of day is investigated. The vertical resolution of Ri is limited by the vertical resolution of the ADCP currents, which is 1 m. Figure 13a shows the temporal evolution of the peak of the PDF of Ri at various depth intervals. For depths $z < -4$ m, the PDF of Ri has a peak at 0.25, which is indicative that this region may be predominantly unstable. For greater depths, -4 m $< z < -14$ m, there is a diurnal structure to the peak of the Richardson number distribution, where Ri is lower during the day than in the evening. The timing of the decrease in Ri varies for each depth interval, with deeper observations decreasing later than shallower ones. Observations of Ri increase

again at $\approx$1800 LMT, coinciding with B_0 becoming negative and destabilizing (Fig. 11).

Another important aspect of Ri is the fraction of occurrences where Ri < 0.25, which we will denote $N_{0.25}$. This fraction is calculated at different depth intervals and is shown in Fig. 13b. For $z < -4$ m, there are a greater number of occurrences of Ri < 0.25 during the day when the diurnal jet is present compared to the same depths at night. This peak is even more apparent when the number of occurrences of Ri < 0.65 (denoted $N_{0.65}$) are considered, which may be more a more appropriate threshold, as this corresponds with the mode of the distribution of Ri (Fig. 13a) and our estimates are limited by the 1-m vertical resolution of velocity. Figure 13c shows the diurnal evolution of $N_{0.65}$ for various depths, which has the same diurnal shape as $N_{0.25}$.

The evolution of stability can be seen from the diurnal evolution of $N_{0.65}$ (Fig. 13c). In the morning, the complex interplay of restratification and the diurnal jet act to increase the occurrence of $N_{0.65}$, indicating a greater occurrence of shear instability. The rate and onset of this increase changes with depth with shallower depths increasing with a greater rate and at earlier times than at larger depths. At 1300 LMT, $N_{0.65}$ reaches a peak for the -6 m $< z < -4$ m depth interval, which suggests that the flow is unstable as the median of Ri drops below 0.65. Through shear instability, the flow entrains the underlying flow that acts to decrease $N_{0.65}$ in the shallow layer and increase $N_{0.65}$ in the deeper layer. This creates a cascade that appears identical to the mechanism described by Smyth et al. (2013), which provides the initial forcing for deep cycle turbulence in the equatorial Pacific. While our Richardson threshold of 0.65 is somewhat arbitrary and larger than the accepted value of 0.25, the fact that the median values of Ri < 1 for our relatively coarse velocity resolution suggests that shear instability is likely to be present.

This peak in $N_{0.25}$ and $N_{0.65}$ can be interpreted as a descent rate. For either critical Richardson number Ri_c, the weighted mean time associated with the peak of N_{Ri_c} is calculated as

$$\langle t_{Ri_c}(z) \rangle = \frac{\int^t t N_{Ri_c} \, dt}{\int^t N_{Ri_c} \, dt} \qquad (17)$$

to determine the descent rate for N_{Ri_c}. The descent rate is then calculated as the change in depth of $\langle t_{Ri_c} \rangle$. The dashed black–white lines in Fig. 14 shows $\langle t_{0.65}(z) \rangle$, which demonstrates a mean descent rate of 2.0 m h^{-1} for depths $z > -12$ m. The descent rate associated with $\langle t_{0.25}(z) \rangle$ was found to be 1.8 m h^{-1}, which is nearly
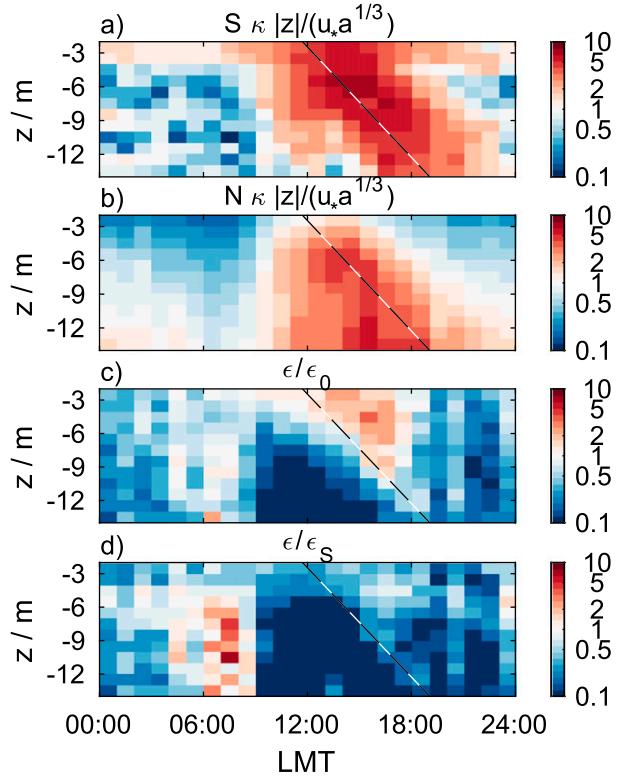
FIG. 14. (a) Diurnally averaged shear S and (b) stratification N normalized by the law of the wall shear and diurnally averaged ε normalized by (c) ε_0 as calculated by (4) and (d) ε_S as calculated by (18). The black–white dashed line shows the mean time of $N_{0.65}$ [$\langle t_{0.65}(z) \rangle$], which corresponds to a descent rate of 2 m h^{-1}.

identical to that obtained with $\langle t_{0.65}(z) \rangle$. This weighted mean time $\langle t_{0.65} \rangle$ appears to be associated with the onset of enhanced $\varepsilon/\varepsilon_0$, as shown in Fig. 14c. Both descent rates are less than the 6 m h^{-1} observed by Smyth et al. (2013) in the equatorial Pacific. It is uncertain as to the cause of the discrepancy in descent rates, but it might be attributed to the presence of the equatorial undercurrent or due to the inertial rotation of the diurnal jet at our latitude.

8. Enhanced shear = enhanced ε?

The region with the greater number of occurrences of Ri < 0.25 coincided with enhanced $\varepsilon/\varepsilon_0$ (Fig. 14c). The depth of enhanced ε was bounded temporally by $\langle t_{0.65}(z) \rangle$ and 1800 LMT and spatially by -10 m $< z <$ 0 m, which is precisely where the diurnal jet occurred. The enhancement of $\varepsilon/\varepsilon_0$ ceased rather abruptly at 1800 LMT at all depths, coinciding with B_0 changing from stabilizing to destabilizing.

This region of enhanced $\varepsilon/\varepsilon_0$ also coincides with a region of enhanced mean shear (Fig. 11c), which would

increase the production of turbulent kinetic energy through (1). The shear is enhanced by a factor of 5 in the descending diurnal jet relative to that expected of wall-bounded shear (Fig. 14a), which is consistent with the estimates of the near-surface shear made by Kudryavtsev and Soloviev (1990) and with our observed values of $\varepsilon/\varepsilon_0$. Using the observed shear, we can define a new normalized dissipation rate:

$$\varepsilon_S = a^{2/3}u_*^2 S + b\frac{B_0 + |B_0|}{2}, \qquad (18)$$

where S is the observed shear [instead of assuming the shear follows the law of the wall scaling as in (4) and the same buoyancy offset is chosen when B_0 is destabilizing]. In (18), the friction velocity is scaled by $a^{1/3}$ to be consistent with (4). Observed values of ε are more consistent with ε_S during the day (Fig. 14d) than ε_0 (Fig. 14c).

Assuming that the primary source for ε is from shear production, then $\varepsilon/\varepsilon_S$ yields an estimate for the in situ Reynolds stress normalized by the surface stress from the wind. Figure 14d shows $\varepsilon/\varepsilon_S$ for the composite day, and it appears that the enhancement in $\varepsilon/\varepsilon_0$ is primarily due to the enhanced shear associated with the diurnal jet. During restratification (and before the onset of shear instability that is shown by the dashed line in Fig. 14), the Reynolds stress, relative to the wind stress, extends to a uniform shallow depth of a few meters and quickly decreases by an order of magnitude as stratification limits the vertical diffusion. However, the peak $N_{0.65}$ corresponds with an increase in $\varepsilon/\varepsilon_S$ before the stratification begins to decrease (Fig. 14b), suggesting that this change is not coming from an increase in the vertical diffusivity but instead is a local source of turbulence. This local source is consistent with shear instability transferring energy from the mean shear into turbulent motions. This increase in $\varepsilon/\varepsilon_S$ corresponds with $\langle t_{0.65}(z)\rangle$, suggesting that the descending shear layer is leaving turbulence and instabilities in its wake.

9. Summary and discussion

Presented here are observations of the diurnal structure of the ocean surface boundary layer (OSBL) obtained in the subtropical North Atlantic during August/September 2012. High-resolution observations in the OSBL were made with the Air–Sea Interaction Profiler (ASIP), an autonomous vertical microstructure profiler that profiles upward to the free surface. The fact that ASIP is autonomous and vertically rising allowed for accurate microstructure observations far from the effects of any ship-induced contamination to the near-surface turbulent processes. ASIP was used in conjunction with

a cloverleaf buoy (the Trèfle) that resolved velocities in the near-surface region. This pairing of instruments allowed for coincident velocity and microstructure measurements of the diurnal jet in the OSBL.

During the campaign, several diurnal warming events were observed due to the low wind speeds and high solar insolation. These diurnal warming events followed a typical pattern with a daytime increase in SST of 0.2° to 0.5°C occurring at close to 1400 local mean time (LMT). The increase in SST was accompanied by an increase in near-surface velocity, that is, a diurnal jet, which began in the along-wind direction each morning and slowly turned cum sole due to the Coriolis force. The magnitude of the diurnal jet was observed to be on the order of $0.1\,\mathrm{m\,s^{-1}}$, consistent with previous observations near this latitude (Price et al. 1986).

Several length scales were investigated associated with the diurnal cycle of SST. The classic Monin–Obukhov length L_{MO} underestimated the boundary layer thickness compared to several different diagnostic length scales. This could be due to the TKE shear being underestimated by the law of the wall model or that L_{MO} never reaches a steady-state due to the constantly changing surface buoyancy flux during the day. The prognostic depth scale of (Price et al. 1986) $\tilde{D}_T \propto L_{\mathrm{MO}}^{1/2}(u_* P_Q)^{1/2}$, where P_Q is a relevant time scale taken to be half of the total daylight hours, was able to predict the minimum boundary layer thickness during the day.

The diurnal jet enhances the near-surface shear relative to that expected for a logarithmic velocity profile. One of the main results of this paper is that the increased shear acts to increase ε, presumably through the production of TKE from the interaction of the Reynolds stress and the mean shear. This process is juxtaposed with the increased stratification acting to reduce the vertical diffusion of the Reynolds stress. Taking into account the observed shear, which is approximately 5 times greater than expected for the observed surface stress, leads to a turbulence scaling (which we denote ε_S), which is more consistent with observations. Assuming that shear production is the predominant source of ε, then the ratio $\varepsilon/\varepsilon_S$ can be interpreted as the Reynolds stress normalized by the surface wind stress. Figure 14d shows that the ratio $\varepsilon/\varepsilon_S$ gives a rapid decrease in the Reynolds stress in the remnant layer during restratification. The depth to which the Reynolds stress falls to 10% of the surface wind stress is nearly constant until the early afternoon, where it increases at depth coinciding with a greater occurrence of $\mathrm{Ri} < 0.25$.

This interpretation, that is, that the reduction in ε is due to a decrease in the Reynolds stress, is slightly different to the conclusions of Smyth et al. (1997), who attributed the decay of ε below a stratified layer as a

result of a decrease in the vertical advection of TKE, while shear production persisted in the remnant layer albeit cut off from surface forcing. The interpretation of Smyth et al. (1997) was based on a lack of correlation between ε, N^2, S^2, and Ri within the remnant layer, and therefore a decrease in shear production was deemed unlikely. However, as we have shown, the stratification above the remnant layer limits the diffusion of the Reynolds stress, and it is this that is separated from the surface. The observed exponential decay of ε cut off from surface forcing (Brainerd and Gregg 1993; Smyth et al. 1997; Callaghan et al. 2014) is also consistent with a decrease in the Reynolds stress, as ε is proportional to the Reynolds stress, rather than a reduction in vertical advection of TKE.

The diurnal jet is also accompanied by a greater occurrence of Ri < 0.25, which is indicative of shear instability. While this increased occurrence is limited to 10% to 20% of the observed values of Ri in the upper 10 m, the 1-m vertical resolution of the ADCP could lead to an underestimate of the shear and hence an overestimate of Ri. It does appear that the conditions are favorable for shear instability, but higher-resolution velocity measurements would be required to confirm this. While the enhanced values of ε appear to be associated with the enhanced shear of the diurnal jet, it may be that shear instability may prove to be an integral part of the enhanced turbulence as it will generate turbulence in addition to the wind stress as the stratification does appear to limit the vertical diffusion of momentum. This statement is at least qualitatively consistent with Fig. 14d, where $\varepsilon/\varepsilon_S$ for $z > -3$ m during the morning, yet increases with depth in the afternoon, coinciding with the greater observations of Ri < 0.65.

One aspect of the diurnal jet that we were unable to clearly address is whether any memory of previous diurnal events exists, as suspected by Woods and Strass (1986), or whether the jet is formed onto a ''clean slate'' as hypothesized by Stommel et al. (1969). Figure 10 shows a very different evolution for the diurnal jet during each day. Deployment three in particular shows the diurnal jet on 09/07 to have characteristics of an inertial oscillation, while the next day has a very strange response with little along-wind increase. This interaction between the inertial and diurnal response can also be seen in the currents throughout the OSBL (Fig. 4), but a much longer time series than this one would be required to investigate this interaction.

These observations present new insight into the complicated processes associated with shallow, stable boundary layers in the ocean. During conditions of low wind and high solar insolation an interesting feedback mechanism occurs, which acts to increase the turbulence intensity relative to the wind forcing. The increased stratification creates a delicate balance between the increased near-surface shear and the limited vertical extent of the constant stress layer to create slightly enhanced values of ε relative to turbulence in neutral buoyancy conditions. This process could be an important component to the air–sea transfer of momentum, heat, and trace gases in tropical regions as the diurnal jet is expected to occur wherever a diurnal temperature variability is observed. The enhanced ε relative to wind forcing is expected to have an impact on estimates of the air–sea transfer of water soluble gases, such as CO_2 and O_2 (Lamont and Scott 1970; Ward et al. 2004; McGillis et al. 2004; Zappa et al. 2007), as a wind stress parameterization would underestimate the gas transfer velocity in regions with large diurnal variability. This enhanced turbulence would lead to an increase in the flux of CO_2 from the sea to the atmosphere as diurnal cycling predominantly occurs in tropical and subtropical regions where the partial pressure of CO_2 is greater in the sea than in the atmosphere.

REFERENCES

Asher, W. E., A. T. Jessup, and D. Clark, 2014: Stable near-surface ocean salinity stratifications due to evaporation observed during STRASSE. *J. Geophys. Res. Oceans*, **119**, 3219–3233, doi:10.1002/2014JC009808.

Belcher, S. E., and Coauthors, 2012: A global perspective on Langmuir turbulence in the ocean surface boundary layer. *Geophys. Res. Lett.*, **39**, L18605, doi:10.1029/2012GL052932.

Bernie, D., S. Woolnough, J. Slingo, and E. Guilyardi, 2005: Modeling diurnal and intraseasonal variability of the ocean mixed layer. *J. Climate*, **18**, 1190–1202, doi:10.1175/JCLI3319.1.

Brainerd, K., and M. Gregg, 1993: Diurnal restratification and turbulence in the oceanic surface mixed layer: 1. Observations. *J. Geophys. Res.*, **98**, 22 645–22 656, doi:10.1029/93JC02297.

——, and ——, 1995: Surface mixed and mixing layer depths. *Deep-Sea Res.*, **42**, 1521–1543, doi:10.1016/0967-0637(95)00068-H.

Caldwell, D. R., R. C. Lien, J. N. Moum, and M. C. Gregg, 1997: Turbulence decay and restratification in the equatorial ocean surface layer following nighttime convection. *J. Phys. Oceanogr.*, **27**, 1120–1132, doi:10.1175/1520-0485(1997)027<1120:TDARIT>2.0.CO;2.

Callaghan, A. H., B. Ward, and J. Vialard, 2014: Influence of surface forcing on near-surface and mixing layer turbulence in the tropical Indian Ocean. *Deep-Sea Res. I*, **94**, 107–123, doi:10.1016/j.dsr.2014.08.009.

Clayson, C. A., and A. S. Bogdanoff, 2013: The effect of diurnal sea surface temperature warming on climatological air–sea fluxes. *J. Climate*, **26**, 2546–2556, doi:10.1175/JCLI-D-12-00062.1.

Craig, P. D., and M. L. Banner, 1994: Modelling wave-enhanced turbulence in the ocean surface layer. *J. Phys. Oceanogr.*, **24**, 2546–2559, doi:10.1175/1520-0485(1994)024<2546:MWETIT>2.0.CO;2.

Cronin, M. F., and W. S. Kessler, 2009: Near-surface shear flow in the tropical Pacific cold tongue front. *J. Phys. Oceanogr.*, **39**, 1200–1215, doi:10.1175/2008JPO4064.1.

D'Asaro, E. A., 1985: The energy flux from the wind to near-inertial motions in the surface mixed layer. *J. Phys. Oceanogr.*, **15**, 1043–1059, doi:10.1175/1520-0485(1985)015<1043:TEFFTW>2.0.CO;2.

——, 2014: Turbulence in the upper-ocean mixed layer. *Annu. Rev. Mar. Sci.*, **6**, 101–115, doi:10.1146/annurev-marine-010213-135138.

——, C. Lee, L. Rainville, R. Harcourt, and L. Thomas, 2011: Enhanced turbulence and energy dissipation at ocean fronts. *Science*, **332**, 318–322, doi:10.1126/science.1201515.

de Boyer Montégut, C., G. Madec, A. S. Fischer, A. Lazar, and D. Iudicone, 2004: Mixed layer depth over the global ocean: An examination of profile data and a profile-based climatology. *J. Geophys. Res.*, **109**, C12003, doi:10.1029/2004JC002378.

Drushka, K., S. T. Gille, and J. Sprintall, 2014: The diurnal salinity cycle in the tropics. *J. Geophys. Res. Oceans*, **119**, 5874–5890, doi:10.1002/2014JC009924.

Fairall, C. W., E. F. Bradley, J. E. Hare, A. A. Grachev, and J. B. Edson, 2003: Bulk parameterization of air–sea fluxes: Updates and verification for the COARE algorithm. *J. Climate*, **16**, 571–591, doi:10.1175/1520-0442(2003)016<0571:BPOASF>2.0.CO;2.

Gargett, A. E., and C. E. Grosch, 2014: Turbulence process domination under the combined forcings of wind stress, the Langmuir vortex force, and surface cooling. *J. Phys. Oceanogr.*, **44**, 44–67, doi:10.1175/JPO-D-13-021.1.

Gill, A. E., 1982: *Atmosphere–Ocean Dynamics*. Academic Press, 662 pp.

Jähne, B., and H. Haußecker, 1998: Air-water gas exchange. *Annu. Rev. Fluid Mech.*, **30**, 443–468, doi:10.1146/annurev.fluid.30.1.443.

Kara, A. B., P. A. Rochford, and H. E. Hurlburt, 2000: An optimal method for ocean mixed layer depth. *J. Geophys. Res.*, **105**, 16 803–16 821, doi:10.1029/2000JC900072.

Kawai, Y., and A. Wada, 2007: Diurnal sea surface temperature variation and its impact on the atmosphere and ocean: A review. *J. Oceanogr.*, **63**, 721–744, doi:10.1007/s10872-007-0063-0.

Kenyon, K. E., 1969: Stokes drift for random gravity waves. *J. Geophys. Res.*, **74**, 6991–6994, doi:10.1029/JC074i028p06991.

Khoo, B., and A. Sonin, 1992: Augmented gas exchange across wind-sheared and shear-free air-water interfaces. *J. Geophys. Res.*, **97**, 14 413–14 415, doi:10.1029/92JC01293.

Kudryavtsev, V. N., and A. V. Soloviev, 1990: Slippery near-surface layer of the ocean arising due to daytime solar heating. *J. Phys. Oceanogr.*, **20**, 617–628, doi:10.1175/1520-0485(1990)020<0617:SNSLOT>2.0.CO;2.

Lamont, J. C., and D. Scott, 1970: An eddy cell model of mass transfer into the surface of a turbulent liquid. *AIChE J.*, **16**, 513–519, doi:10.1002/aic.690160403.

Large, W. G., J. C. McWilliams, and S. C. Doney, 1994: Ocean vertical mixing: A review and a model with a nonlocal boundary layer parameterization. *Rev. Geophys.*, **32**, 363–403, doi:10.1029/94RG01872.

Lombardo, C. P., and M. C. Gregg, 1989: Similarity scaling of viscous and thermal dissipation in a convecting surface boundary layer. *J. Geophys. Res.*, **94**, 6273–6284, doi:10.1029/JC094iC05p06273.

McGillis, W. R., and Coauthors, 2004: Air-sea CO2 exchange in the equatorial Pacific. *J. Geophys. Res.*, **109**, C08S02, doi:10.1029/2003JC002256.

McWilliams, J. C., P. P. Sullivan, and C. H. Moeng, 1997: Langmuir turbulence in the ocean. *J. Fluid Mech.*, **334**, 1–30, doi:10.1017/S0022112096004375.

Miles, J., 1961: On the stability of heterogeneous shear flows. *J. Fluid Mech.*, **10**, 496–508, doi:10.1017/S0022112061000305.

Nicholson, D. P., S. T. Wilson, S. C. Doney, and D. M. Karl, 2015: Quantifying subtropical North Pacific Gyre mixed layer primary productivity from Seaglider observations of diel oxygen cycles. *Geophys. Res. Lett.*, **42**, 4032–4039, doi:10.1002/2015GL063065.

Osborn, T. R., 1974: Vertical profiling of velocity microstructure. *J. Phys. Oceanogr.*, **4**, 109–115, doi:10.1175/1520-0485(1974)004<0109:VPOVM>2.0.CO;2.

——, 1980: Estimates of the local rate of vertical diffusion from dissipation measurements. *J. Phys. Oceanogr.*, **10**, 83–89, doi:10.1175/1520-0485(1980)010<0083:EOTLRO>2.0.CO;2.

Paulson, C. A., and J. J. Simpson, 1977: Irradiance measurements in the upper ocean. *J. Phys. Oceanogr.*, **7**, 952–956, doi:10.1175/1520-0485(1977)007<0952:IMITUO>2.0.CO;2.

Plueddemann, A. J., and R. A. Weller, 1999: Structure and evolution of the oceanic surface boundary layer during the surface waves processes program. *J. Mar. Syst.*, **21**, 85–102, doi:10.1016/S0924-7963(99)00007-X.

Price, J. F., R. A. Weller, and R. Pinkel, 1986: Diurnal cycling: Observations and models of the upper ocean response to diurnal heating, cooling, and wind mixing. *J. Geophys. Res.*, **91**, 8411–8427, doi:10.1029/JC091iC07p08411.

Rascle, N., F. Ardhuin, and E. A. Terray, 2006: Drift and mixing under the ocean surface: A coherent one-dimensional description with application to unstratified conditions. *J. Geophys. Res.*, **111**, C03016, doi:10.1029/2005JC003004.

Reverdin, G., and Coauthors, 2015: Surface salinity in the North Atlantic Subtropical Gyre: During the STRASSE/SPURS summer 2012 cruise. *Oceanography*, **28**, 114–123, doi:10.5670/oceanog.2015.09.

Shay, T. J., and M. C. Gregg, 1986: Convectively driven turbulent mixing in the upper ocean. *J. Phys. Oceanogr.*, **16**, 1777–1798, doi:10.1175/1520-0485(1986)016<1777:CDTMIT>2.0.CO;2.

Smyth, W. D., P. O. Zavialov, and J. N. Moum, 1997: Decay of turbulence in the upper ocean following sudden isolation from surface forcing. *J. Phys. Oceanogr.*, **27**, 810–822, doi:10.1175/1520-0485(1997)027<0810:DOTITU>2.0.CO;2.

——, J. Moum, L. Li, and S. Thorpe, 2013: Diurnal shear instability, the descent of the surface shear layer, and the deep cycle of equatorial turbulence. *J. Phys. Oceanogr.*, **43**, 2432–2455, doi:10.1175/JPO-D-13-089.1.

Soloviev, A. V., and R. Lukas, 2014: *The Near-Surface Layer of the Ocean*. 2nd ed. Springer, 552 pp.

Stevens, C., B. Ward, C. Law, and M. Walkington, 2011: Surface layer mixing during the SAGE ocean fertilization

experiment. *Deep-Sea Res. II*, **58**, 776–785, doi:10.1016/j.dsr2.2010.10.017.

Stommel, H., K. Saunders, W. Simmons, and J. Cooper, 1969: Observations of the diurnal thermocline. *Deep-Sea Res.*, **16**, 269–284.

Sutherland, G., B. Ward, and K. H. Christensen, 2013: Wave-turbulence scaling in the ocean mixed layer. *Ocean Sci.*, **9**, 597–608, doi:10.5194/os-9-597-2013.

——, K. H. Christensen, and B. Ward, 2014a: Evaluating Langmuir turbulence parameterizations in the ocean surface boundary layer. *J. Geophys. Res. Oceans*, **119**, 1899–1910, doi:10.1002/2013JC009537.

——, G. Reverdin, L. Marié, and B. Ward, 2014b: Mixed and mixing layer depths in the ocean surface boundary layer. *Geophys. Res. Lett.*, **41**, 8469–8476, doi:10.1002/2014GL061939.

Takahashi, T., and Coauthors, 2009: Climatological mean and decadal change in surface ocean pCO2, and net sea–air CO_2 flux over the global oceans. *Deep-Sea Res. II*, **56**, 554–577, doi:10.1016/j.dsr2.2008.12.009.

Wain, D. J., J. M. Lilly, A. H. Callaghan, I. Yashayaev, and B. Ward, 2015: A breaking internal wave in the surface ocean boundary layer. *J. Geophys. Res. Oceans*, **120**, 4151–4161, doi:10.1002/2014JC010416.

Ward, B., 2006: Near-surface ocean temperature. *J. Geophys. Res.*, **111**, C02005, doi:10.1029/2004JC002689.

——, R. Wanninkhof, W. R. McGillis, A. T. Jessup, M. D. DeGrandpre, J. E. Hare, and J. B. Edson, 2004: Biases in the air-sea flux of CO_2 resulting from ocean surface temperature gradients. *J. Geophys. Res.*, **109**, C08S08, doi:10.1029/2003JC001800.

——, T. Fristedt, A. H. Callaghan, G. Sutherland, X. Sanchez, J. Vialard, and A. ten Doeschate, 2014: The Air–Sea Interaction Profiler (ASIP): An autonomous upwardly rising profiler for microstructure measurements in the upper ocean. *J. Atmos. Oceanic Technol.*, **31**, 2246–2267, doi:10.1175/JTECH-D-14-00010.1.

Webb, A., and B. Fox-Kemper, 2011: Wave spectral moments and Stokes drift estimation. *Ocean Modell.*, **40**, 273–288, doi:10.1016/j.ocemod.2011.08.007.

Weller, R. A., and A. J. Plueddemann, 1996: Observations of the vertical structure of the oceanic boundary layer. *J. Geophys. Res.*, **101**, 8789–8806, doi:10.1029/96JC00206.

——, S. Majumder, and A. Tandon, 2014: Diurnal restratification events in the southeast Pacific trade wind regime. *J. Phys. Oceanogr.*, **44**, 2569–2587, doi:10.1175/JPO-D-14-0026.1.

Woods, J. D., 1968: Wave induced shear instabilities in the summer thermocline. *J. Fluid Mech.*, **32**, 791–800, doi:10.1017/S0022112068001035.

——, and V. Strass, 1986: The response of the upper ocean to solar heating. II: The wind-driven current. *Quart. J. Roy. Meteor. Soc.*, **112**, 29–42, doi:10.1002/qj.49711247103.

Zappa, C. J., W. R. McGillis, P. A. Raymond, J. B. Edson, E. J. Hintsa, H. J. Zemmelink, J. W. H. Dacey, and D. T. Ho, 2007: Environmental turbulent mixing controls of air-water gas exchange in marine and aquatic systems. *Geophys. Res. Lett.*, **34**, L10601, doi:10.1029/2006GL028790.